Monthly Notices of the ROYAL ASTRONOMICAL SOCIETY

MNRAS **497,** 572–580 (2020) doi:10.1093/mnras/staa1951
Advance Access publication 2020 July 7

Probing the high-z IGM with the hyperfine transition of $^3He^+$

Shivan Khullar,[1,2,3] Qingbo Ma,[4] Philipp Busch,[1,5,6] Benedetta Ciardi,[1★] Marius B. Eide[1] and Koki Kakiichi[7]

[1]*Max-Planck-Institut für Astrophysik, Karl-Schwarzschild-Str. 1, D-85748 Garching, Germany*
[2]*Research School of Astronomy and Astrophysics, Australian National University, Canberra ACT 2611, Australia*
[3]*Department of Physics, Goa Campus, Birla Institute of Technology and Science, Pilani, Rajasthan 333031, India*
[4]*Guizhou Provincial Key Laboratory of Radio Astronomy and Data Processing, Guizhou Normal University, Guiyang 550001, PR China*
[5]*Department of Natural Science, The Open University of Israel, 1 University Road, PO Box 808, Raanana 43107, Israel*
[6]*Department of Physics, The Technion, Haifa 3200003, Israel*
[7]*Department of Physics and Astronomy, University College London, London WC1E 6BT, UK*

Accepted 2020 June 30. Received 2020 June 29; in original form 2019 August 2

ABSTRACT

The hyperfine transition of $^3He^+$ at 3.5 cm has been thought as a probe of the high-z IGM, since it offers a unique insight into the evolution of the helium component of the gas, as well as potentially give an independent constraint on the 21 cm signal from neutral hydrogen. In this paper, we use radiative transfer simulations of reionization driven by sources such as stars, X-ray binaries, accreting black holes and shock heated interstellar medium, and simulations of a high-z quasar to characterize the signal and analyse its prospects of detection. We find that the peak of the signal lies in the range $\sim$1–50 μK for both environments, but while around the quasar it is always in emission, in the case of cosmic reionization a brief period of absorption is expected. As the evolution of He II is determined by stars, we find that it is not possible to distinguish reionization histories driven by more energetic sources. On the other hand, while a bright QSO produces a signal in 21 cm that is very similar to the one from a large collection of galaxies, its signature in 3.5 cm is very peculiar and could be a powerful probe to identify the presence of the QSO. We analyse the prospects of the signal's detectability using SKA1-mid as our reference telescope. We find that the noise power spectrum dominates over the power spectrum of the signal, although a modest signal-to-noise ratio can be obtained when the wavenumber bin width and the survey volume are sufficiently large.

Key words: radiative transfer – galaxies: high-redshift – (galaxies:) intergalactic medium – (galaxies:) quasars: general – (cosmology:) dark ages, reionization, first stars.

1 INTRODUCTION

The reionization of hydrogen and helium in the intergalactic medium (IGM) at redshifts $z \gtrsim 6$ and $z \gtrsim 2.5$, respectively, is the subject of continued investigations (for a review, see Ciardi & Ferrara 2005; Morales & Wyithe 2010; Pritchard & Loeb 2012; Loeb & Furlanetto 2013). Helium reionization is considered to be the last major phase change in the Universe. While the radiation from stellar type sources responsible for hydrogen reionization singly ionize helium as well, photons with higher energies are required to ionize helium fully. In fact, theoretical models (e.g. Compostella, Cantalupo & Porciani 2014; La Plante & Trac 2016), as well as observations (e.g. Worseck et al. 2011), indicate that helium reionization is driven by Quasi Stellar Objects (or quasars; QSOs).

While QSOs' spectra are routinely used to probe the final phases of hydrogen (e.g. Becker, Bolton & Lidz 2015) as well as helium (e.g. Worseck et al. 2016) reionization, little observational constraint is available on their history. The hyperfine transition of neutral hydrogen (H I), with a rest-frame frequency of 1.42 GHz (21 cm), is a promising probe of the evolution of H reionization (for a review, see Furlanetto, Oh & Briggs 2006). Several ongoing observational efforts have been made in this respect. Among these, the LOw Frequency ARray[1] (LOFAR), the Murchison Widefield Array[2] (MWA), the Hydrogen Epoch of Reionization Array[3] (HERA), the Precision Array for Probing the Epoch of Reionization[4] (PAPER), and the upcoming Square Kilometer Array[5] (SKA). While efforts to probe the high-z IGM have focused extensively on the 21 cm line, the hyperfine transition of $^3He^+$ at 8.66 GHz (3.5 cm) also offers a unique insight into some astrophysical phenomena prevalent in the early universe (Furlanetto et al. 2006; Bagla & Loeb 2009; McQuinn & Switzer 2009; Takeuchi, Zaroubi & Sugiyama 2014; Vasiliev, Sethi & Shchekinov 2019). In addition to being a probe

★ E-mail: ciardi@mpa-garching.mpg.de

[1] www.lofar.org
[2] http://www.mwatelescope.org
[3] https://reionization.org
[4] http://eor.berkeley.edu
[5] https://www.skatelescope.org

of the high-z evolution of the helium component of gas, Bagla & Loeb (2009) suggested that this feature could also in principle be used to obtain independent constraints on the 21 cm signal, because the evolution of both H II and He II are driven by stellar-type sources during the epoch of (hydrogen) reionization, and thus the 21 cm and 3.5 cm signals are expected to be anticorrelated at these redshifts. Finally, in a QSO-dominated reionization scenario (e.g. Madau & Haardt 2015; Hassan et al. 2018), the abundance of He II is much lower than in a standard model because of the hard spectrum of QSOs. This means that, in principle, the strength of the 3.5 cm signal can constrain the type of sources dominating the reionization process, and potentially even their relative importance.

Although the abundance of He II is much smaller than that of H II, the above authors have suggested that the $^3He^+$ hyperfine transition offers some advantages over the 21 cm line, which are summarized as follows: (i) as its rest-frame frequency is considerably higher than the corresponding frequency for H, observations of this signal would suffer from less severe foreground contamination; and (ii) the spontaneous decay rate of the $^3He^+$ transition is ∼680 times larger, thus boosting the signal. However, the prospects for the detection of this signal are severely limited with current telescopes. Although several radio telescopes are operational in the relevant frequency range, probably the best chance to detect the 3.5 cm signal lies with SKA.

Although Bagla & Loeb (2009) have evaluated the expected signal with a semi-analytic approach, a more rigorous modelling has yet to be done which accounts for the evolution of He II (the thorough analysis of Takeuchi et al. 2014 was concentrated at lower redshift and still lacked a full radiative transfer). Here, we revisit this problem employing the simulations of reionization described in Eide et al. (2018, hereafter E18) and Eide et al. 2020 (submitted, hereafter E20), which model both H and He reionization as driven by stellar-type sources, accreting nuclear black holes (BH), X-ray binaries (XRBs), and shock-heated interstellar medium (ISM). We will repeat the same analysis concentrating on the environment surrounding the high-z quasar described in Kakiichi et al. (2017, hereafter K17).

The rest of the paper is structured as follows. In Section 2, we describe the simulations presented in E18, E20, and K17, and the methodology used to calculate the $^3He^+$ signal from such simulations. In Section 3, we present the results of our analysis, and we summarize our findings and highlight the main conclusions of our study in Section 4.

2 SIMULATIONS AND METHOD

In this work, we will evaluate the signal associated with the hyperfine transition of the $^3He^+$ both on cosmological scales and around a high-z QSO. The simulations used here are those described in E18 and E20 for the cosmological signal, and those discussed in K17 for the QSO environment. Here, we outline their main characteristics and refer the readers to the original papers for more details.

2.1 Simulations of cosmic reionization

Outputs of the MassiveBlack-II (MBII; Khandai et al. 2015), a high-resolution cosmological SPH simulation, are combined with population synthesis modelling of ionizing sources and post-processed with the multifrequency 3D radiative transfer code CRASH (e.g. Ciardi et al. 2001; Maselli, Ferrara & Ciardi 2003; Maselli, Ciardi & Kanekar 2009;Graziani, Maselli, and Ciardi 2013; Graziani, Ciardi & Glatzle 2018) to model hydrogen and helium reionization. The MBII simulation has been run using P-GADGET (see Springel 2005 for an earlier version of the code) and tracks stellar populations, galaxies, accreting and dormant BHs as well as their properties like age, star formation rate, metallicity, mass, accretion rate, etc. The simulation is performed in the WMAP7 ΛCDM cosmology (Komatsu et al. 2011), has a box length of $100h^{-1}$ cMpc and 2×1792^3 gas and dark matter particles, with a mass of $m_{\rm gas} = 2.2 \times 10^6\, h^{-1}\, {\rm M}_\odot$ and $m_{\rm DM} = 1.1 \times 10^7\, h^{-1}\, {\rm M}_\odot$, respectively. For outputs with redshift in the range $z = 6$–20, the gas, temperature and ionization fractions fields, as well as the sources of ionizing photons, have been mapped on to $N = 256^3$ grids to be post-processed with CRASH, assuming an escape fraction of UV photons ($13.6\ {\rm eV} < h\nu < 200\ {\rm eV}$) of 15 per cent. The source types included in the radiative transfer simulation are stars, XRBs, accreting nuclear BHs, and bremsstrahlung from shock heated ISM. For more information on the sources and their effects on the IGM, we refer the reader to E18 and E20.

2.2 Simulations of high-z QSO

Similarly to the model of reionization described above, a hydrodynamical simulation of the IGM run with GADGET-3 has been post-processed with CRASH to investigate the environment surrounding a high-z QSO. The simulation adopts cosmological parameters consistent with WMAP9 results (Hinshaw et al. 2013), has a box length of $50h^{-1}$ cMpc, and contains 2×512^3 gas and dark matter particles, corresponding to a mass of $m_{\rm gas} = 1.2 \times 10^7\, h^{-1}\, {\rm M}_\odot$ and $m_{\rm DM} = 5.53 \times 10^7\, h^{-1}\, {\rm M}_\odot$, respectively. By design, the simulation box is centred on the largest halo, having a mass of $1.34 \times 10^{10} h^{-1}\, {\rm M}_\odot$ at $z = 10$. For outputs in the redshift range $z = 15$–10, the gas and temperature fields are mapped on to grids with $N = 256^3$ cells and fed as input to CRASH to solve for the radiative transfer of UV photons emitted by the stellar sources. At $z = 10$, we assume that a QSO turns on in the centre of the most massive halo and its much harder radiation (in this case we follow the RT also in the soft X-ray regime, i.e. $200\ {\rm eV} < h\nu < 2\ {\rm keV}$) is evolved for a time corresponding to the lifetime of the QSO. For further details about the source model and its impact on the ionization and thermal state of the QSO environment, we refer the reader to K17.

2.3 $^3He^+$ signal

The simulations of cosmic reionization and QSO's environment described in the previous sections provide, among others, the spatial and temporal distribution of gas temperature, $T_{\rm gas}$, as well as fractions of H II, He II, and He III (i.e. $x_{\rm H\,II}$, $x_{\rm He\,II}$, and $x_{\rm He\,III}$, respectively). The gas number density, $n_{\rm gas}$, is instead taken directly from the hydrodynamic simulations. From these quantities, the differential brightness temperature associated with the hyperfine transition of $^3He^+$, $\delta T_{\rm b,^3He}$, can be evaluated in each cell of the simulated volume as (see equation 61 of Furlanetto et al. 2006):

$$\delta T_{\rm b,^3He} \approx 0.5106\, x_{\rm He\,II}(1+\delta)\left(1-\frac{T_{\rm CMB}}{T_{\rm s}}\right) \times \left(\frac{[^3{\rm He/H}]}{10^{-5}}\right)\left(\frac{\Omega_{\rm b}\, h^2}{0.0223}\right)\sqrt{\frac{\Omega_{\rm m}}{0.24}}(1+z)^{1/2}\,\mu{\rm K}, \quad (1)$$

where $\delta = (n_{\rm gas} - \bar{n}_{\rm gas})/\bar{n}_{\rm gas}$ is the gas overdensity with $\bar{n}_{\rm gas}$ mean gas number density of the whole box, $x_{\rm He\,II}$ is the fraction of He II, $T_{\rm CMB} = 2.725(1+z)$ K is the CMB temperature at redshift z, $T_{\rm s}$ is the spin temperature, $\Omega_{\rm b}$ and $\Omega_{\rm m}$ are the baryonic and matter density parameters and $h = H_0/100$, where H_0 (in units of km s^{-1} Mpc^{-1}) is the Hubble constant. The abundance of ^{3}He relative to that of H, $[^3{\rm He/H}] \approx 10^{-5}$, is dictated by the big bang nucleosynthesis (equation

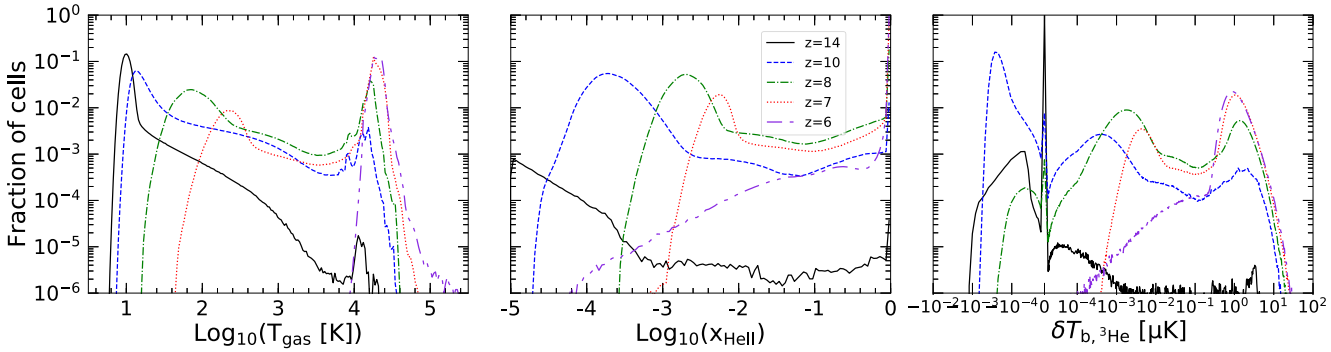

Figure 1. From left to right, the panels refer to the distribution of the gas temperature, $T_{\rm gas}$, of the He II fraction, $x_{\rm He\,II}$, and of the differential brightness temperature, $\delta T_{\rm b,^3He}$, for the 256^3 cells in the cosmological simulation of cosmic reionization as described in Section 2.1. The lines refer to $z = 14$ (black solid), 10 (blue dashed), 8 (green dash–dotted), 7 (red dotted), and 6 (purple dash-dot–dotted).

6 of Coc 2016). Note that in the equation above we have made the common assumption that $\frac{H(z)}{(1+z)(\mathrm{d}v_\parallel/\mathrm{d}r_\parallel)} \sim 1$, and throughout the paper we will also assume that $T_{\rm s} \sim T_{\rm gas}$ (see the Appendix for a discussion on the latter assumption).

As the power spectrum (PS) is a quantity that can be inferred directly from radio interferometric observations, we will also estimate the PS of the $^3He^+$ signal as expected from our simulations. We evaluate the PS of the differential brightness temperature field as

$$P(\boldsymbol{k}) = \langle \delta T_{\rm b,^3He}(\boldsymbol{k})\, \delta T_{\rm b,^3He}(\boldsymbol{k})^* \rangle, \tag{2}$$

where $\delta T_{\rm b,^3He}(\boldsymbol{k})$ is the Fourier transform of the differential brightness temperature field, and $\delta T_{\rm b,^3He}(\boldsymbol{k})^*$ is the complex conjugate of $\delta T_{\rm b,^3He}(\boldsymbol{k})$. We additionally define the quantity $\Delta^2_{^3\rm He}$ (in units of $[\mu\mathrm{K}]^2$) as

$$\Delta^2_{^3\rm He} = \frac{k^3}{2\pi^2} P(\boldsymbol{k}). \tag{3}$$

3 RESULTS

In this section, we will briefly discuss the properties of the output fields of the simulations mentioned in Section 2, the differential brightness temperature field and the PS of the $^3He^+$ signal at different redshifts.

3.1 Cosmic reionization

While we refer the reader to E18 and E20 for an extensive discussion of the evolution of the IGM temperature and ionization state, here we briefly highlight what is strictly necessary for this study.

In Fig. 1 (left-hand panel), we show the distribution of the gas temperature. At high redshift, it presents two peaks: the strongest one is at $T_{\rm gas} \sim 10$ K,[6] indicating that most of the gas is still cold, while a second considerably weaker peak is visible at $T_{\rm gas} \sim 10^4$ K, corresponding to the gas that has already been ionized by the few sources present at these redshifts. As the redshift decreases and more, larger sources appear increasing the size and number of ionized regions, the first peak shifts towards larger temperatures and becomes less relevant, until it completely disappears by $z \sim 6$ when all gas is ionized. At the same time, the second peak becomes predominant and shifts as well towards larger values as the helium component of the gas gets ionized in appreciable quantities.

[6]Note that this reflects the numerical temperature floor of the simulations.

Since the first ionization potential of He at 24.6 eV is close to the 13.6 eV for H, all H ionizing sources in the simulation singly ionize He as well, and as a consequence the distribution of $x_{\rm He\,II}$ and $x_{\rm H\,II}$ resemble each other very closely, except at low redshift when an appreciable fraction of $x_{\rm He\,III}$ (the second ionization potential of He is 54.4 eV) starts to appear.[7] For this reason, in Fig. 1 (central panel) we show only the distribution of $x_{\rm He\,II}$, which, similarly to the gas temperature, presents two peaks, one at low ionization which shifts towards larger values with decreasing redshift (and eventually disappears), and one corresponding to full ionization, which becomes increasingly important as reionization proceeds.[8]

The corresponding distribution of the differential brightness temperature field is shown in the right-hand panel of Fig. 1. Due to the small amount of singly ionized He, at high redshifts $\delta T_{\rm b,^3He}$, is mostly zero. Nevertheless, the signal can be observed in both absorption and emission with values varying between $\sim -10^{-3}$ and ~ 5 μK. The negative values are associated with partially ionized cells whose temperature has not been raised above that of the CMB (see also Fig. 2) and which contribute to the cold peak observed in the left-hand panel of the figure. The peak in the negative values grows from $z = 14$ to $z = 10$, since there are more partially ionized cells at $z = 10$ than $z = 14$, as is also seen in the central panel of Fig. 1. As the redshift decreases, more helium gets ionized and the gas heated, causing the cells with negative and zero values of $\delta T_{\rm b,^3He}$ to diminish and eventually disappear when reionization is complete by $z \sim 6$. At the same time, most of the signal becomes in emission and increases in intensity.

For a better understanding of the dependence of the differential brightness temperature on $T_{\rm gas}$ and $x_{\rm He\,II}$, in Fig. 2 we plot a phase diagram at various redshifts. The value of the differential brightness temperature for each of the 256^3 cells has been plotted as a function of the corresponding $x_{\rm He\,II}$ and $T_{\rm gas}$ values. At redshifts $z \geq 10$, the main contribution to the differential brightness temperature comes, at negative values, from gas which is colder than $T_{\rm CMB}$ and poorly ionized ($x_{\rm He\,II} \leq 10^{-3}$), and, at positive values, from highly ionized hot gas. As z decreases, the gas transitions from the cold to the hot peak that was seen in Fig. 1 while $x_{\rm He\,II}$ increases, resulting in a signal which is predominantly (and eventually totally) in emission. Once

[7]For more information on the sources' spectra and their effect on the physical state of the IGM, we refer the reader to E18 and E20.

[8]Note that the Monte Carlo method adopted here assures convergence of the results down to a value of the ionization fraction of 10^{-5}.

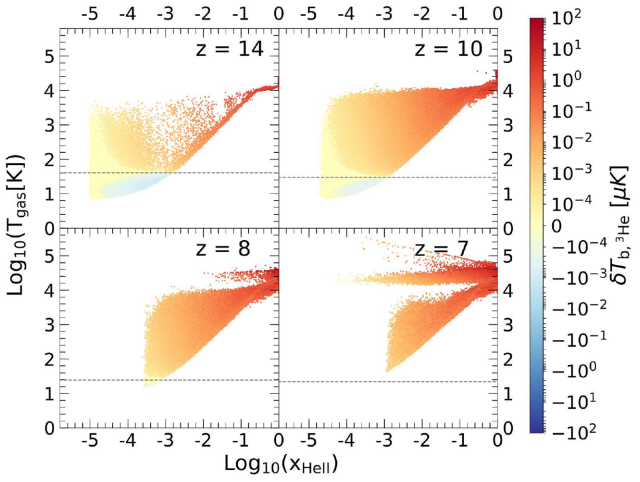

Figure 2. Differential brightness temperature, $\delta T_{\rm b,^3He}$, for the 256^3 cells in the cosmological simulation of cosmic reionization as described in Section 2.1 as a function of the corresponding $T_{\rm gas}$ and $x_{\rm He\,II}$ values. The panels refer to $z = 14$ (top left), 10 (top right), 8 (bottom left), and 7 (bottom right). The horizontal lines indicate $T_{\rm CMB}$.

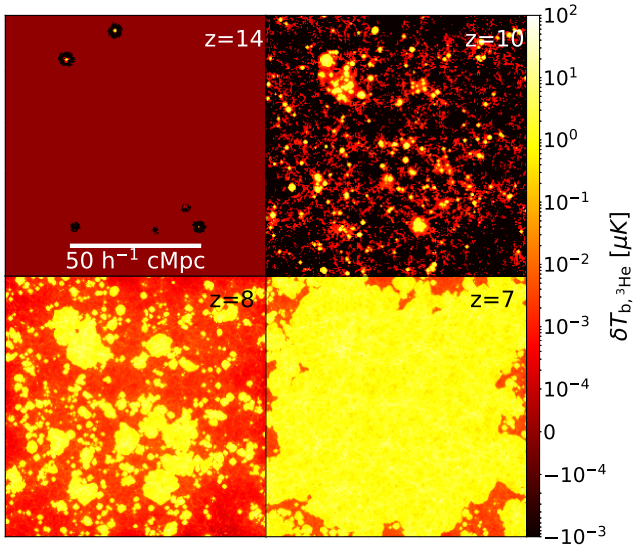

Figure 3. A slice of the differential brightness temperature field (in μK) in the cosmological simulation of cosmic reionization as described in Section 2.1 at $z = 14$ (top left-hand panel), 10 (top right), 8 (bottom left), and 7 (bottom right).

$T_{\rm gas} \gg 10^4$ K, helium becomes doubly ionized and consequently $x_{\rm He\,II}$ decreases.

In Fig. 3, we show maps of $\delta T_{\rm b,^3He}$ in a slice of the simulation box. At redshift $z \geq 10$, the IGM is either predominantly neutral or very lowly ionized (as a result of hard ionizing photons with a large mean free path like the ones emanating from energetic sources such as XRBs, ISM, and BHs) and thus in most of the IGM $\delta T_{\rm b,^3He}$ is zero or in the range $[-10^{-4}, -10^{-3}]$ μK. As the redshift decreases, the differential brightness temperature values increase and reach a maximum of $\delta T_{\rm b,^3He} \sim 25$ μK; the amount of He II on large scales increases (as the ionized regions grow in size and number) and the $^3He^+$ signal can only be seen in emission.

In Fig. 4, we show $\Delta^2_{^3\rm He}$ as a function of the wavenumber k. At high redshifts, the intensity of the PS is extremely low since there

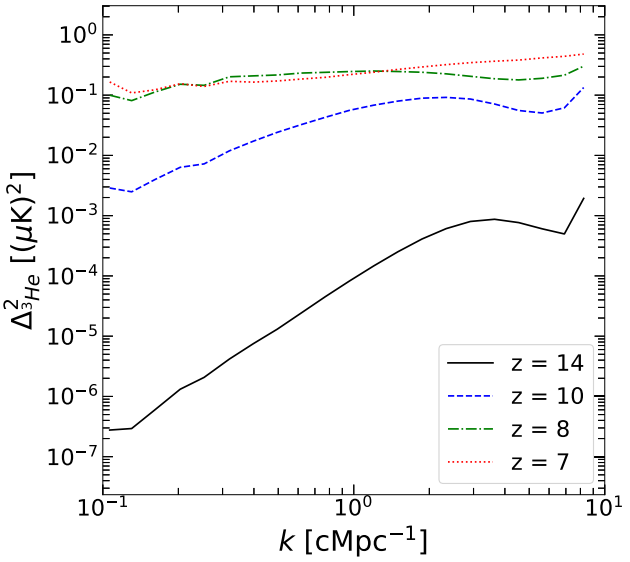

Figure 4. PS of the $^3He^+$ signal for the simulation of cosmic reionization as described in Section 2.1 at redshift $z = 14$ (black solid line), 10 (blue dashed line), 8 (green dash–dotted line), and 7 (red dotted line).

is very little He II in the simulation box and, as it is concentrated in small ionized regions around the early galaxies, $\Delta^2_{^3\rm He}$ behaves like white Gaussian noise. However, as reionization proceeds and more He II gets ionized, we observe a general increase of power, in particular at small k values. As a result, the shape of the PS becomes flatter with decreasing redshift, until the power is almost the same on all scales at $z < 7$ when $x_{\rm He\,II} \sim 1$ everywhere. Although not shown here, we expect the shape of the He II 3.5 cm signal to be similar to that of the H II 21 cm signal, as the morphology of the H II and He II bubbles resemble each other in the absence of strong 54.4 eV ionizing sources.

3.2 High-z QSO

As in the case of the simulations of cosmic reionization, we refer the reader to K17 for an extensive discussion of the QSO's environment and its impact on the ionization and thermal state of the IGM, while we only briefly highlight what is strictly necessary for this study. In Fig. 5 (left-hand panel), we show the distribution of the gas temperature for different values of the QSO's lifetime, $t_{\rm QSO}$. Similarly to what noted in the previous section, initially two clear peaks are observable, one associated with the cold gas that has not yet been reached by ionizing photons, and the second at $T_{\rm gas} \sim 12\,500$ K, accounting for the fully ionized gas surrounding the central QSO and/or nearby galaxies. As expected, the first (second) peak becomes less (more) prominent for larger $t_{\rm QSO}$, as an increasing number of cells gets fully ionized. A peak at intermediate values is also visible, which corresponds to the temperature of the central He III bubble within the He II region. The peak at the highest temperature values remains and grows more prominent until $t_{\rm QSO} = 5 \times 10^7$ yr. Between $t_{\rm QSO} = 5 \times 10^7$ yr and $t_{\rm QSO} = 10^8$ yr, the temperature of the central bubble increases, leading to a broadening of the peak at the highest temperature values. As a result, the distinction between the two remaining peaks becomes less prominent.

For reasons mentioned in the previous section, He is singly ionized along with H. However, for a bright QSO as the one considered here, the ionizing radiation is energetic enough to doubly ionize He appreciably, leading to the formation of a ring of He II around the

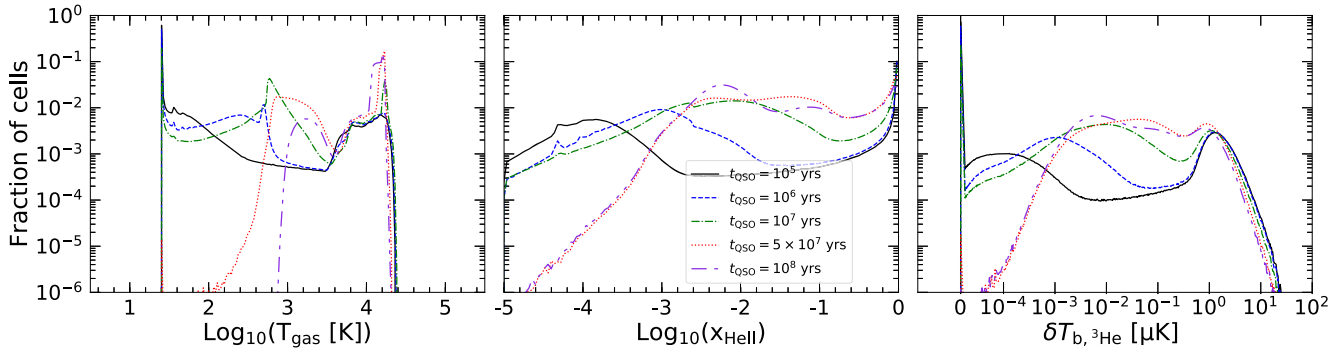

Figure 5. From left to right, the panels refer to the distribution of the gas temperature, $T_{\rm gas}$, of the He II fraction, $x_{\rm He\,II}$, and of the differential brightness temperature, $\delta T_{\rm b,^3He}$, for the 256^3 cells in the simulation of a high-z QSO as described in section Section 2.2. The lines refer to a quasar's lifetime of $t_{\rm QSO} = 10^5$ yr (black solid), 10^6 yr (blue dashed), 10^7 yr (green dash–dotted), 5×10^7 yr (red dotted), and 10^8 yr (purple dash-dot–dotted).

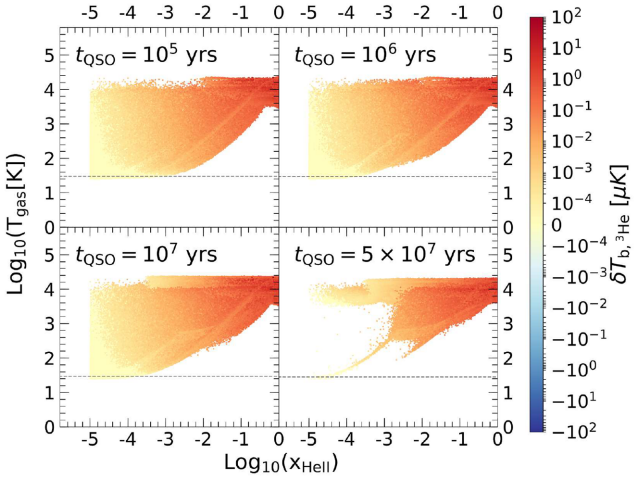

Figure 6. Differential brightness temperature, $\delta T_{\rm b,^3He}$, for the 256^3 cells in the simulation of a high-z QSO as described in Section 2.2 as a function of the corresponding $T_{\rm gas}$ and $x_{\rm He\,II}$ values. The panels refer to $t_{\rm QSO} = 10^5$ yr (top left), 10^7 yr (bottom left), and 5×10^7 yr (bottom right). The horizontal lines indicate $T_{\rm CMB}$.

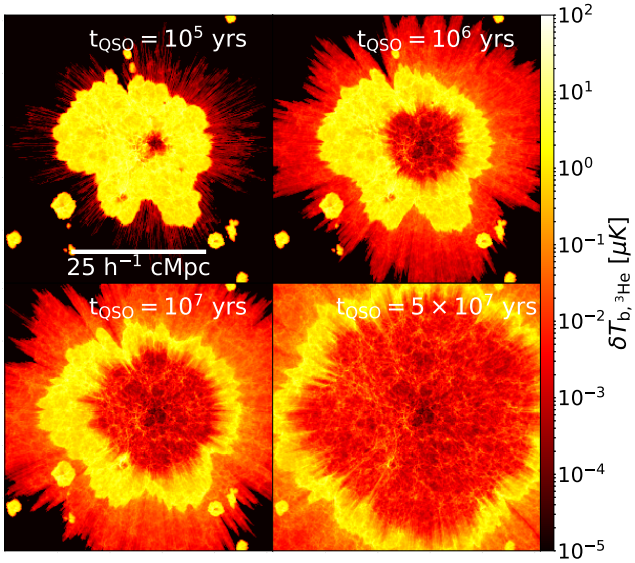

Figure 7. A slice of the differential brightness temperature field (in μK) in the simulation of a high-z QSO as described in Section 2.2 at $t_{\rm QSO} = 10^5$ yr (top left), 10^6 yr (top right), 10^7 yr (bottom left), and 5×10^7 yr (bottom right).

QSO (see K17). In the central panel of Fig. 5, we show the distribution of $x_{\rm He\,II}$. Unlike the cosmic reionization simulations discussed earlier in which the fraction of cells with $x_{\rm He\,II} \sim 1$ tends to unity, this is not observed here, as a substantial fraction of cells is being converted to doubly ionized helium. For the same reason, the peak at intermediate values of the ionization fraction is not as prominent as those seen in Fig. 1 (central panel).

The corresponding distribution of the differential brightness temperature field is shown in Fig. 5 (right-hand panel). Due to the small amount of singly ionized He, initially $\delta T_{\rm b,^3He}$ is mostly zero. However, unlike in the cosmic reionization simulation, the signal can only be observed in emission with virtually nothing in absorption. The distribution resembles that of the corresponding $x_{\rm He\,II}$ values, with the distinction between the peaks becoming less prominent with increasing QSO lifetime. The signal does, however, decrease slightly in intensity as redshift decreases, following the behaviour of the gas temperature.

In Fig. 6, we plot a phase diagram illustrating the dependence of the differential brightness temperature on $T_{\rm gas}$ and $x_{\rm He\,II}$. As the QSO gets older, the predominant contribution to the differential brightness temperature comes from highly ionized hot gas and the signal cannot be seen in absorption. The higher brightness of the QSO compared to that of the various BHs in the reionization simulations manifests itself also through the presence of hot gas with low $x_{\rm He\,II}$.

In Fig. 7, we show maps of $\delta T_{\rm b,^3He}$ in a slice of the simulation box. During the initial stages in the evolution of the QSO, the ionized region surrounding it is mostly made of He II, which can be seen as an almost homogeneous bubble with $x_{\rm He\,II} \sim 1$ and $\delta T_{\rm b,^3He}$ as high as ∼50 μK. However, as the QSO age increases, a region of doubly ionized helium rapidly forms and expands within the He II bubble, leaving only a ring of outward expanding singly ionized helium, the thickness of which decreases with time. The peak of the emission arises from this ring, reaching a maximum of $\delta T_{\rm b,^3He} \sim 50$ μK. The more energetic photons emitted by the QSO, due to their longer mean free path, are able to propagate beyond this region and to partially ionize helium, giving rise to a signal of $\sim 10^{-3}$ μK. Finally, the internal region, in which most helium is in its doubly ionized state, results in a differential brightness temperature between $\sim 10^{-3}$ and 10^{-2} μK.

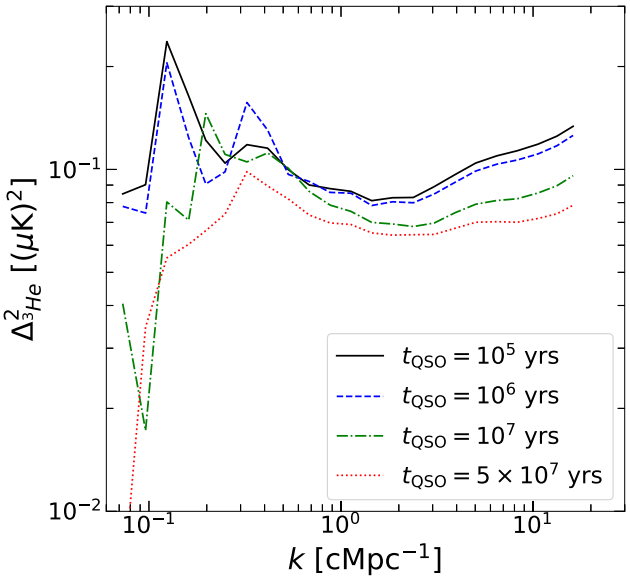

Figure 8. PS of the $^3He^+$ signal from the QSO simulations corresponding to QSO lifetimes of $t_{QSO} = 10^5$ yr (black solid line), 10^6 yr (blue dashed), 10^7 yr (green dash–dotted), and 5×10^7 yr (red dotted).

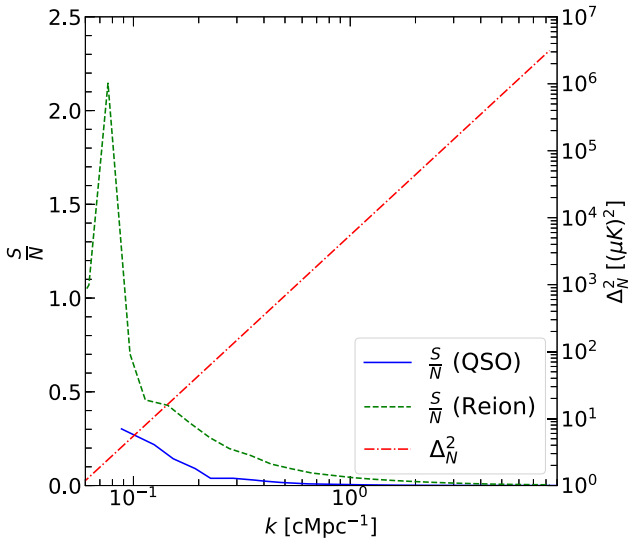

Figure 9. S/N (left y-axis) and the equivalent Δ^2_N (right y-axis) as a function of k. The green dashed and blue solid lines refer to the S/N of the $^3He^+$ signal (from equation 6) in the cosmic reionization simulation at $z = 7$ and the high-z QSO simulation with $t_{QSO} = 10^5$ yr, respectively. The red dash–dotted line indicates the dimensionless PS of the noise for our chosen reference telescope, SKA1-mid, with a frequency band $B = 0.1$ MHz, an integration time $t_{int} = 3000$ h, a k bin width $k_{width} = 0.23{*}k$ cMpc^{-1}, and a survey volume $V = 10^8$ cMpc^3.

In Fig. 8, we show the PS of the differential brightness temperature. The shape of the PS remains similar throughout the QSO's evolution, although it becomes flatter with time, i.e. the power is concentrated at the smallest and largest scales encompassed by the simulations, with an inflection at $k \sim 1$ cMpc^{-1}. As the QSO gets older, the He II region surrounding it grows in size while a smaller He III region is formed closer to the QSO, resulting in an increase of power on large scales and a decrease on small scales. Eventually, though, the power decreases on all scales as less He II is present. The overall magnitude of the intensity of the PS is similar to the one obtained from the simulations of cosmic reionization described in Section 2.1.

3.3 Detectability

In this section, we analyse the prospects of detecting the $^3He^+$ signal, which corresponds to a frequency of 0.58–1.24 GHz in the redshift range $z = 6$–14. Thus, we take SKA1-mid[9] as the reference telescope. SKA1-mid is designed to cover the frequency range of 0.35–14 GHz, with a total of 190 15-m dishes and 64 MeerKAT dishes, i.e. $N_{dish} = 254$. It is expected to have a sensitivity $S_N = 1600\,m^2\,K^{-1}$ in the frequency range $\nu_0 = 0.95$–1.76 GHz and $S_N = 992\,m^2\,K^{-1}$ in the frequency range of $\nu_0 = 0.35$–1.05 GHz. To test the detectability of the He II signal during the EoR, we assume all the dishes to be in a core of radius $R = 4$ km. The flux noise of SKA1-mid can be written as (Wilson, Rohlfs & Hüttemeister 2009):

$$\sigma_N = \frac{2k_B T_{sys}}{A_{eff}\sqrt{N_{dish}(N_{dish}-1)Bt_{int}}}, \tag{4}$$

where k_B is the Boltzmann constant, T_{sys} is the system temperature of the telescope, A_{eff} is the effective collecting area of one dish, N_{dish} is the number of dishes, B is the frequency bandwidth, and t_{int} is the integration time. Using the Rayleigh–Jeans relation $\sigma_N = 2k_B T_N \Gamma_b \lambda^{-2}$, and the definition of sensitivity of the telescope $S_N = N_{dish}{*}A_{eff}/T_{sys}$, the rms of the brightness temperature of the noise can be written as

$$\delta T_N = \frac{\lambda^2}{S_N/N_{dish}\Gamma_b\sqrt{N_{dish}(N_{dish}-1)Bt_{int}}}, \tag{5}$$

where λ is the wavelength and $\Gamma_b = 1.33(\lambda/R)^2$. Assuming white noise, its PS is $N(k) = \delta T_N^2 V_N$, where V_N is the volume covered by the noise pixel. We assume $B = 0.1$ MHz and $t_{int} = 3000$ h. The S/N of the PS can be expressed as

$$\left(\frac{S}{N}\right)^2 = \frac{4\pi k^2 k_{width} V}{(2\pi)^3}\frac{P(k)^2}{[P(k)+N(k)]^2}, \tag{6}$$

where $\theta = \lambda/R$, V is the volume of the survey, and k_{width} is the width of the k bin.

In Fig. 9, we plot the quantity Δ^2_N using equations (2) and (3) for the differential brightness temperature of the noise alongside the S/Ns for the power spectra of the simulations of cosmic reionization (Fig. 4) at $z = 7$. The S/Ns are plotted using a reference k bin width $k_{width} = 0.23{*}k$ cMpc^{-1} (i.e. $\delta\log_{10}(k) = 0.1$), and a survey volume $V = 10^8$ cMpc^3, which corresponds to a survey area $\Omega = 55.4$ deg^2 at $z = 7$, or equivalently, $\Omega = 51.5$ deg^2 at $z = 8$ with a slice width equal to 100 cMpc. Comparing Δ^2_N to the PS of the signal plotted in Figs 4 and 8, it is clear that the noise PS on most scales is orders of magnitude higher than the corresponding values for the PS of the signal. However, for large enough k bin widths and survey volumes, the S/N of a few can be reached up to $\sim$0.5 cMpc^{-1} for the cosmic reionization simulation. These scales are not covered by the QSO simulation (because of the smaller box) but also in this case we expect similar values. Thus, our analysis does not rule out the possibility that telescopes in the future might be able to detect the signal.

[9] https://www.skatelescope.org/wp-content/uploads/2014/11/SKA-TEL-SKO-0000002-AG-BD-DD-Rev01-SKA1_System_Baseline_Design.pdf

4 DISCUSSION AND CONCLUSIONS

In this paper, we have evaluated the expected signal from the $^3He^+$ hyperfine transition using hydrodynamical and radiative transfer simulations of cosmic reionization that include different source types (stars, accreting nuclear BHs, XRBs and shock heated ISM; see E18 and E20), as well as of the environment of a bright QSO at $z = 10$ (see K17). In both cases, we find that the peak of the signal is expected to lie in the range of ∼1–50 μK. While in the QSO's environment the signal is always in emission, in the case of cosmic reionization we observe a brief period in which the signal is expected to be also in absorption, with a maximum value of $\sim -10^{-3}$ μK. This is due to gas far away from sources, which gets partially ionized by energetic photons emitted by either the ISM or XRBs.

We note that these results are valid under the assumption of coupling between the spin and gas temperature. Although a proper assessment of the coupling strength requires a detailed He II Ly α radiative transfer, our approximate approach in the Appendix indicates that the He II Ly α background produced in the cosmic reionization simulations is at least an order of magnitude below the one required for a full coupling through scattering. This suggests that, unless additional sources contributing to the background (such as a binary component in the stellar spectrum, a more abundant population of BHs at high redshift, the Ly α flux from excitation by X-ray photons) are included, an efficient coupling could be expected only in very high density pockets of gas through collisions, or in the vicinity of strong sources such as BHs (see also Vasiliev et al. 2019), where the local radiation dominates over the background (see e.g. Ciardi et al. 2000).

It is important to note that it is not possible to distinguish reionization histories from different source types as we do not find any appreciable difference in the PS between simulations containing only galactic stellar sources and the ones described in Section 2.1 containing also XRBs, BHs, and ISM. This happens because most of the signal is dominated by gas with $x_{\rm He\,II} \sim 1$, which in standard scenarios is driven by stellar type sources (see also discussions in E18 and E20). On the other hand, we do find that the $^3He^+$ signal might be a powerful probe to identify the presence of a bright high-z QSO. In fact, the 21-cm signal associated with the environment of a QSO is very similar to the one from a large collection of galaxies (see Ma et al. in preparation), because of the similarities in the associated ionized regions. On the contrary, the $^3He^+$ signal is very peculiar, as it can be seen by comparing the bottom left-hand panel of Figs 7–10, where the differential brightness temperature is shown in the absence of the QSO contribution to reionization. In this case, the characteristic 'hole' in the emission associated with the presence of He III is missing due to the softer spectrum of stellar-type sources, which are not able to fully ionize He. This also suggests that, in principle, the 3.5 cm signal could be used to distinguish a QSO from a stellar-dominated reionization scenario, and potentially constrain their relative importance.

Finally, we find that the $^3He^+$ signal is weak and the prospects of its detection are presently severely limited. Using the SKA1-mid as our reference telescope, we find that the noise PS dominates over the PS of the $^3He^+$ signal. However, for a large enough k bin width and survey volume, an S/N of a few could be reached on the largest scales. Thus, our analysis leaves the possibility open for future telescopes to detect the $^3He^+$ hyperfine transition signal.

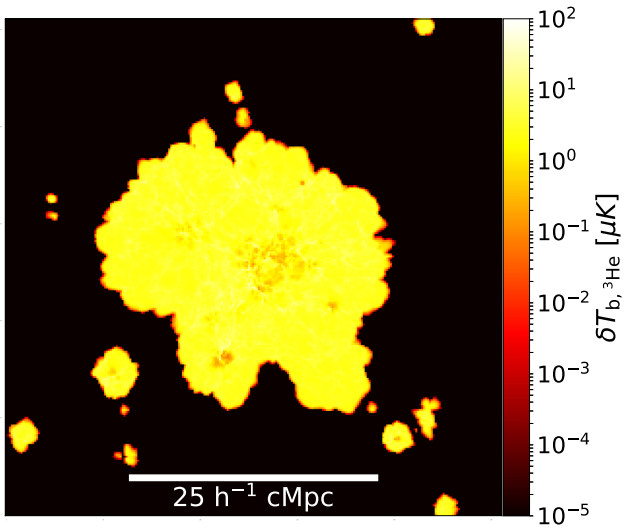

Figure 10. A slice of the $^3He^+$ differential brightness temperature field (in μK) in the simulation of the high-z QSO described in Section 2.2, but including only the galactic contribution to the ionizing radiation, i.e. the QSO is not turned on. The map is shown at a time corresponding to the bottom left-hand panel of Fig. 7.

ACKNOWLEDGEMENTS

The authors would like to thank Aniket Bhagwat for helpful discussions, and Enrico Garaldi and an anonymous referee for their insightful comments. MBE is grateful the Institute of Theoretical Astrophysics at UiO for their kind hospitality. QM is supported by the innovation and entrepreneurial project of Guizhou province for high-level overseas talents [grant no. (2019)02], the National Natural Science Foundation of China (grant no. 11903010), and the Science and Technology Fund of Guizhou Province [grant no. (2020)1Y020)].

DATA AVAILABILITY

No new data were generated or analysed in support of this research.

REFERENCES

Bagla J. S., Loeb A., 2009, preprint(arXiv:0905.1698)
Becker G. D., Bolton J. S., Lidz A., 2015, PASA, 32, e045
Chuzhoy L., Shapiro P. R., 2006, ApJ, 651, 1
Ciardi B., Ferrara A., 2005, Space Sci. Rev., 116, 625
Ciardi B., Madau P., 2003, ApJ, 596, 1
Ciardi B., Ferrara A., Governato F., Jenkins A., 2000, MNRAS, 314, 611
Ciardi B., Ferrara A., Marri S., Raimondo G., 2001, MNRAS, 324, 381
Coc A., 2016, J. Phys. Conf. Ser., 665, 012001
Compostella M., Cantalupo S., Porciani C., 2014, MNRAS, 445, 4186
Deguchi S., Watson W. D., 1985, ApJ, 290, 578
Eide M. B., Graziani L., Ciardi B., Feng Y., Kakiichi K., Di Matteo T., 2018, MNRAS, 476, 1174 (E18)
Eide M. B.,, Ciardi B., Graziani L., Busch p., Feng Y., Di Matteo T., 2020, MNRAS, submitted
Field G. B., 1958, Proc. IRE, 46, 240
Furlanetto S. R., Oh S. P., Briggs F. H., 2006, Phys. Rep., 433, 181
Graziani L., Maselli A., Ciardi B., 2013, MNRAS, 431, 711
Graziani L., Ciardi B., Glatzle M., 2018, MNRAS, 479, 4320
Hassan S., Davé R., Mitra S., Finlator K., Ciardi B., Santos M. G., 2018, MNRAS, 473, 227
Hinshaw G. et al., 2013, ApJS, 208, 19
Kakiichi K., Graziani L., Ciardi B., Meiksin A., Compostella M., Eide M. B., Zaroubi S., 2017, MNRAS, 468, 3718 (K17)
Khandai N., Di Matteo T., Croft R., Wilkins S., Feng Y., Tucker E., DeGraf C., Liu M.-S., 2015, MNRAS, 450, 1349
Komatsu E. et al., 2011, ApJS, 192, 18

La Plante P., Trac H., 2016, ApJ, 828, 90
Loeb A., Furlanetto S. R., 2013, The First Galaxies in the Universe, Princeton Univ. Press, Princeton NJ, USA
Madau P., Haardt F., 2015, ApJ, 813, L8
Maselli A., Ferrara A., Ciardi B., 2003, MNRAS, 345, 379
Maselli A., Ciardi B., Kanekar A., 2009, MNRAS, 393, 171
McQuinn M., Switzer E. R., 2009, Phys. Rev. D, 80, 063010
Morales M. F., Wyithe J. S. B., 2010, ARA&A, 48, 127
Pritchard J. R., Furlanetto S. R., 2007, MNRAS, 376, 1680
Pritchard J. R., Loeb A., 2012, Rep. Prog. Phys., 75, 086901
Springel V., 2005, MNRAS, 364, 1105
Takeuchi Y., Zaroubi S., Sugiyama N., 2014, MNRAS, 444, 2236
Vasiliev E. O., Sethi S. K., Shchekinov Y. A., 2019, MNRAS, 490, 5057
Wilson T. L., Rohlfs K., Hüttemeister S., 2009, Tools of Radio Astronomy. Springer-Verlag, Berlin, Germany
Worseck G. et al., 2011, ApJ, 733, L24
Worseck G., Prochaska J. X., Hennawi J. F., McQuinn M., 2016, ApJ, 825, 144

APPENDIX: COUPLING TO THE GAS TEMPERATURE

The spin temperature of $^3He^+$ is determined by the collisional process and He II Ly α radiative transfer via the He II analogue of the Wouthuysen–Field effect (Bagla & Loeb 2009; McQuinn & Switzer 2009; Takeuchi et al. 2014):

$$T_s = \frac{T_{CMB} + y_c T_k + y_\alpha T_\alpha}{1 + y_c + y_\alpha}, \quad \text{(A1)}$$

where y_c and y_α are the collisional and He II Ly α coupling coefficients, respectively, T_α is the colour temperature of the radiation field near the $^3He^+$ Ly α line, and T_k is the kinetic temperature of the gas.[10]

As for the 21 cm line from neutral hydrogen, collisional coupling is efficient exclusively at high density and low temperatures ($y_c \propto n_e\, T_k^{-1.5}$, with n_e electron number density). In the typical conditions of the IGM, this is true only at $z \gtrsim 20$, as can be seen from Fig. A1, where no gas is found with $y_c > 10^{-3}$ at the redshifts of interest here. Similar results are found from the QSO's environment in Fig. A2. It should be noted that, employing simulations capable of resolving smaller scales, these would also capture pockets of higher density gas (e.g. Lyman limit systems), where the value of the collisional coefficient would be proportionally higher. It should also be noted that a 21 cm signal would be produced also without full coupling, albeit with a smaller intensity.

The $^3He^+$ line can also be pumped through the He II analogue of the Wouthuysen–Field mechanism, i.e. by scattering off of UV photons at He II Ly α line (40.8 eV). However, in this case the efficiency of the Wouthuysen–Field mechanism is less clear than for H I. Because of the presence of more abundant $^4He^+$ by a factor of $y_{^4He}/y_{^3He} \sim 7.5 \times 10^3$ ($y_{^3He} \sim 10^{-5}$ and $y_{^4He} = 0.083$ are the primordial abundance ratio by number of helium isotope 3 and 4 relative to H atoms), most of He II Ly α scatterings is caused by $^4He^+$. This led previous studies (e.g. Chuzhoy & Shapiro 2006; McQuinn & Switzer 2009) to conclude that the Wouthuysen–Field mechanism is inefficient for $^3He^+$. However, this ignores the effect of multiple scatterings of He II Ly α photons, which have a high He II Gunn–Peterson optical depth of $\tau_{GP}^{He\,II} = (y_{^4He}/4)\tau_{GP}^{H\,II} \sim 1.6 \times 10^4[(1+z)/11]^{3/2}$. This can effectively compensate the low abundance of $^3He^+$, because $(y_{^3He}/y_{^4He})\tau_{GP}^{He\,II} \sim 2$, and thus boost the previous estimates of the He II Wouthuysen–Field effect by a factor of 2.

Moreover, such investigations have considered the Wouthuysen–Field coupling strength by a homogeneous UV background. While this might be more relevant for a typical region of the diffuse IGM with stars only, in the presence of more energetic sources, these provide an additional reservoir of high energy UV photons bluewards of the He II Ly α line (>40.8 eV). Therefore, the Wouthuysen–Field coupling strength may not be as low as previously estimated, although

[10]Note that because we adopt the formulation of the spin temperature of Takeuchi et al. (2014), which is based on the original Field (1958) paper, the collisional and Ly α coupling coefficients y_c and y_α are not equivalent to the x_c and x_α employed by Furlanetto et al. (2006) and McQuinn & Switzer (2009).

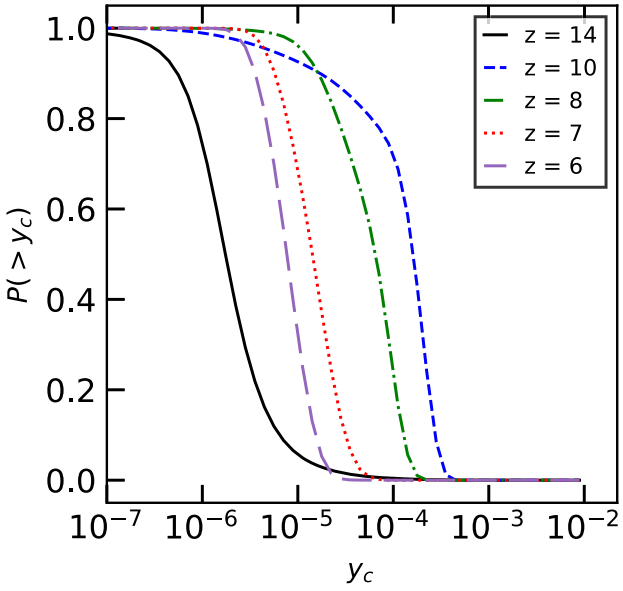

Figure A1. Probability for gas to have a collisional coupling coefficient larger than y_c for the simulation of cosmic reionization as described in Section 2.1 at $z = 14$ (black solid line), 10 (blue dashed), 8 (green dotted dashed), 7 (red dotted), and 6 (purple long dashed).

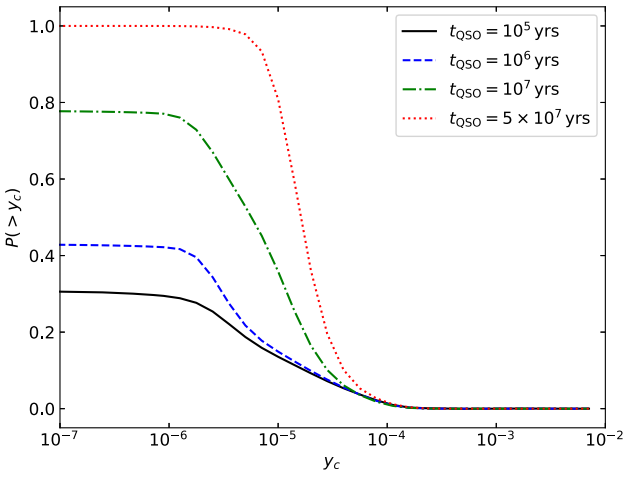

Figure A2. Probability for gas to have a collisional coupling coefficient larger than y_c for the QSO simulations corresponding to QSO lifetimes of $t_{QSO} = 10^5$ yr (black solid line), 10^6 yr (blue dashed), 10^7 yr (green dash–dotted), and 5×10^7 yr (red dotted).

a detailed modelling by solving the He II Ly α radiative transfer in an expanding universe is necessary to draw a quantitative conclusion, which is beyond the scope of the present investigation.

For a rough estimate of the He II Ly α coupling strength, we follow Ciardi & Madau (2003, equations 2–4) and evaluate the minimum Ly α background, $J_{\rm th}^{\rm He\,II}$, required for the coupling to be effective, finding[11]

$$J_{\alpha}^{\rm He\,II} > J_{\rm th}^{\rm He\,II} \approx 10^{-20}(1+z)\ {\rm erg\,cm^{-2}\,s^{-1}\,Hz^{-1}\,sr^{-1}}, \quad \text{(A2)}$$

which is about one order of magnitude higher than for efficient Ly α coupling for H.

In Fig. A3, we show the redshift evolution of the He II Ly α background obtained from our simulations of cosmic reionization. We see that at any time the background is at least an order of magnitude lower than what required for a full coupling. The addition of the contribution from sources that have not been included in this work, such as a binary component in the stellar spectrum, a more abundant population of BHs at high redshift, the Ly α flux from excitation by X-ray photons (see e.g. Pritchard & Furlanetto 2007), could raise the He Ly α background above $J_{\rm th}^{\rm He\,II}$, but, as mentioned earlier, a proper quantitative assessment of the Ly α coupling requires a more accurate physical modelling.

Note also that a full coupling of the colour temperature of the He II Ly α radiation field to the spin temperature is not necessary to observe the differential brightness temperature in emission, as long as the coupling rises the colour temperature sufficiently above the CMB temperature (e.g. Deguchi & Watson 1985).

Finally, as the radiation from local sources is expected to dominate over the background radiation, in particular at the higher redshifts before a strong background had time to build up (see e.g. Ciardi et al. 2000), the best (possibly only) locations where the signal could be detected would be in the vicinity of the sources, in particular BHs (see also Vasiliev et al. 2019).

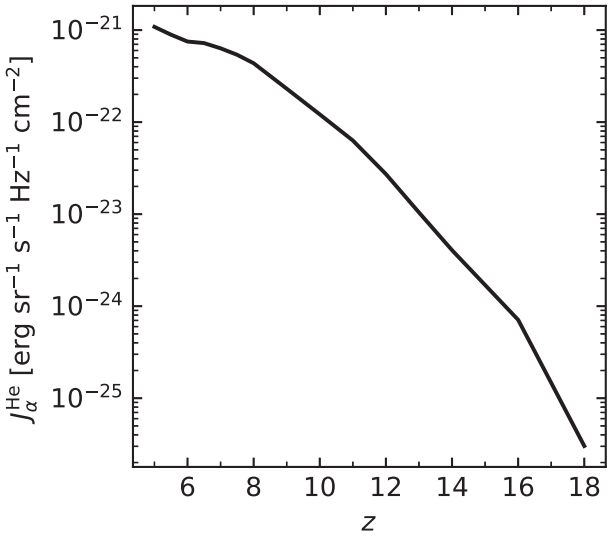

Figure A3. Evolution of the He II Ly α background for the simulation of cosmic reionization.

[11] The values of the various constants are taken from Takeuchi et al. (2014).

This paper has been typeset from a TEX/LATEX file prepared by the author.